



Core-mantle boundary topography and its relation to the viscosity structure of the lowermost mantle

Björn H. Heyn ^{a,*}, Clinton P. Conrad ^a, Reidar G. Trønnes ^{a,b}

^a Centre for Earth Evolution and Dynamics (CEED), University of Oslo, Norway

^b Natural History Museum, University of Oslo, Norway



ARTICLE INFO

Article history:

Received 11 October 2019

Received in revised form 18 May 2020

Accepted 21 May 2020

Available online xxxx

Editor: M. Ishii

Keywords:

core-mantle boundary topography

mantle plumes

large low shear velocity provinces

mantle structure

thermochemical piles

dynamic topography

ABSTRACT

Two large areas of anomalously low seismic velocities are visible in all tomographic models of the lowermost mantle. Depending on the density structure of these Large Low Shear Velocity Provinces (LLSVPs), the core-mantle boundary (CMB) will deform upwards or downwards due to isostatic and dynamic topography, the latter being sensitive to the viscosity structure of the lowermost mantle. Heterogeneities in the viscosity structure, although difficult to constrain, might be especially important if the LLSVPs are thermochemical piles with elevated intrinsic viscosity as suggested by mineral physics. Based on numerical models, we identify a short-wavelength (about 80–120 km wide, up to a few km deep) topographic depression that forms around the pile edges if the pile is more viscous than the surrounding mantle. The depression forms when a wedge of thermal boundary layer material becomes compressed against the viscous pile, and is enhanced by relative uplift of the CMB beneath the pile by plumes rising above it. The depth and asymmetry of the depression constrain the magnitude of the viscosity contrast between pile and the surrounding mantle. Furthermore, (periodic) plume initiation and pile collapse at the pile margin systematically modify the characteristic depression, with a maximum in asymmetry and depth at the time of plume initiation. Core-reflected waves or scattered energy may be used to detect this topographic signature of stiff thermochemical piles at the base of the mantle.

© 2020 The Author(s). Published by Elsevier B.V. This is an open access article under the CC BY license (<http://creativecommons.org/licenses/by/4.0/>).

1. Introduction

Although the presence of a dominant degree-2 structure in seismic velocities of the lowermost mantle (Fig. 1) is well established (e.g., Dziewonski et al., 2010), the origins, and therefore the properties, of the Large Low Shear Velocity Provinces (LLSVPs) are still under debate (e.g., McNamara and Zhong, 2004; Davies et al., 2012; Li et al., 2014; Mulyukova et al., 2015; Trønnes et al., 2019). Some studies suggest a purely thermal origin of the observed velocity anomalies (e.g., Schubert et al., 2012; Davies et al., 2012), while most geodynamic models include thermochemical piles of dense material to explain the observations (e.g., McNamara and Zhong, 2004; Li et al., 2014; Mulyukova et al., 2015). Seismic observations, such as sharp and steep boundaries, are often used to support the hypothesis of a chemical origin of the LLSVPs (see review by McNamara, 2019, and references therein), yet they can possibly also be explained by strong temperature gradients (Schubert et al., 2012; Davies et al., 2012).

One way to discriminate between thermal and thermochemical structures is via their density anomaly relative to the ambient mantle, which is negative for thermal upwellings and neutral to positive in the case of thermochemical piles. Estimated densities of LLSVPs from normal mode data and Earth's solid tides range from neutral or even slightly reduced density (Koelemeijer et al., 2017) to a density excess of 0.5–1% and 1–1.5% in the lowermost 300–400 km and 150–200 km above the CMB, respectively (Lau et al., 2017). These estimates include both the effect of thermal expansion and a potential compositional density increase. Moreover, there are two possible candidate materials for thermochemical piles with different properties: dense and presumably viscous primordial iron-rich bridgmanite (Williams et al., 2015; Heyn et al., 2018; Trønnes et al., 2019), or recycled oceanic crust (Li and McNamara, 2013; Mulyukova et al., 2015). Because basaltic material has higher bulk modulus than peridotite, its intrinsic density excess will decrease with increasing depth through the lower mantle, leading to the suggestion of a composite LLSVP structure with a dense basal layer beneath a more unstable accumulation of recycled oceanic crust (Ballmer et al., 2016; Torsvik et al., 2016; Trønnes et al., 2019).

* Corresponding author at: Centre for Earth Evolution and Dynamics (CEED), University of Oslo, Sem Sælands vei 2A, 0371 Oslo, Norway.

E-mail address: b.h.heyn@geo.uio.no (B.H. Heyn).

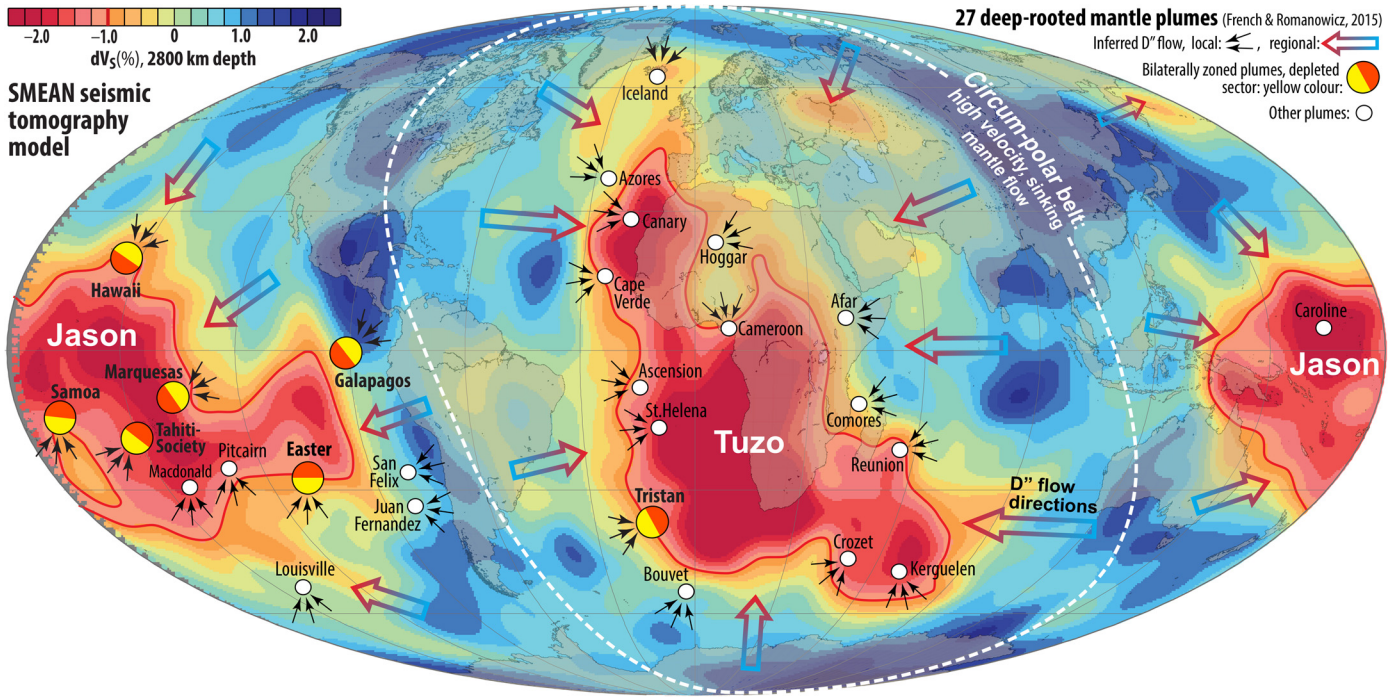


Fig. 1. Tomography model SMEAN (Becker and Boschi, 2002) at 2800 km depth, showing the two LLSVPs and the circumpolar belt of subducted material surrounding them. The deep-rooted plumes, identified by French and Romanowicz (2015), are plotted as circles. Seven of them show bilateral zonation with enriched (red) and depleted (yellow) trends oriented towards and away from the LLSVP interiors, respectively (Harpp et al., 2014; Torsvik et al., 2016, and references therein). Lateral flow towards the LLSVPs is indicated by thick arrows, with local flow towards rising plumes shown as small black arrows. The likely presence of post-bridgmanite in the cool circumpolar belt (blue areas) is expected to reduce the viscosity by 3–4 orders of magnitude (Ammann et al., 2010). This mineralogically-based viscosity decrease will be superimposed on the effect of thermal viscosity reduction in the lowermost mantle, potentially erasing any “memory” of distinct slabs and facilitating the lateral spreading of the cold material. The resulting flow towards the LLSVPs will likely be almost evenly distributed, and directed roughly perpendicular to the LLSVP margins (large arrows). At plume roots, flow will be locally focussed, increasing the average regional flow rate in the vicinity of rising or forming plumes. Thus, a 2-D spherical annulus geometry (90-degree section, Fig. 2) oriented perpendicular to the circumpolar belt should capture this pile-ward flow along the CMB, and it may underestimate the localized flow towards the pile in the locations of plumes. (For interpretation of the colors in the figure(s), the reader is referred to the web version of this article.)

The viscosity of these lithologies will presumably be strongly reduced if post-bridgmanite is present (Ammann et al., 2010). In a recent study based on seismic data, Koelemeijer et al. (2018) inferred that post-bridgmanite is present at about 300 km above the CMB even in the areas of LLSVPs. This is consistent with mineral physics data suggesting that post-bridgmanite may be compositionally stabilized in basaltic material even for higher temperatures, including the conditions that may be expected in the unstable upper part of (composite) LLSVPs (Trønnes et al., 2019). Consequently, as compositionally distinct pile material can exhibit a range of different excess densities, discrimination between thermal and thermochemical LLSVPs based only on density is not straightforward. Details about the viscosity structure in the lowermost mantle would, together with density estimates, provide important insight into the thermal vs. thermochemical nature of the LLSVPs. Unfortunately, we have no direct way of measuring viscosity in the lowermost mantle.

The presence of two thermochemical piles at the base of the mantle should affect flow patterns in the deep Earth. Conrad et al. (2013) have shown that there has been persistent upwelling above the LLSVP regions for at least 250 Myr. This stable upwelling is consistent with a stable pattern of downwelling flow within the circumpolar belt of subducted slabs, which drives lateral flow radially towards the LLSVPs (Fig. 1). This flow is also consistent with the reconstructed eruption sites of Large Igneous Provinces (LIPs) and kimberlites, both related to deep-rooted mantle plumes, which have been shown to cluster around the margins of the LLSVPs (Torsvik et al., 2016; Doubrovine et al., 2016), although the correlation has been questioned (e.g., Austermann et al., 2014). This proximity of plumes to the LLSVP margins can be explained by mantle flow along the CMB towards the pile. The flow is forced upwards

at the edges of dense piles Fig. 1, triggering plumes (Steinberger and Torsvik, 2012; Torsvik et al., 2016; Heyn et al., 2018, 2020).

These density and flow patterns induce steady long-wavelength topography on the CMB. In particular, the isostatic load due to mass (e.g. dense piles) and the dynamic pressure associated with sinking or rising flow exert radial stresses on the boundary between the mantle and the liquid outer core. The amplitude of the resulting deflection depends on the density and viscosity of the material, as well as its velocity. As for the Earth's surface, these stresses are expressed as dynamic topography, with positive topography being associated with light material and rising flow (Fig. 2c), while dense sinking material causes depressions (Lassak et al., 2007; Steinberger and Holme, 2008; Yoshida, 2008; Deschamps et al., 2017). Consequently, core-mantle boundary topography can be used as a proxy to investigate flow in the lowermost mantle as well as certain material properties such as the viscosity and density structures of a (potentially) thermochemical pile (Lassak et al., 2007, 2010; Deschamps et al., 2017).

Core-mantle boundary topography may also impact core flow and the Earth's dynamo. It has been suggested that the topography of the CMB may cause a torque in core flow and thus result in exchange of angular momentum between the mantle and the core (Le Mouël et al., 2006; Roberts and Aurnou, 2012; Ding and Chao, 2018; Glane and Buffett, 2018; Burmann and Noir, 2018). This exchange, potentially strengthened by the presence of stable stratification of the outer core (Glane and Buffett, 2018), has been invoked to explain periodic changes in length-of-day (Roberts and Aurnou, 2012; Ding and Chao, 2018; Glane and Buffett, 2018). Profiles of seismic velocities and geochemical data both indicate that a light stagnant layer (the E-layer) may indeed be present within Earth's outer core (e.g. review by Trønnes et al., 2019, and ref-

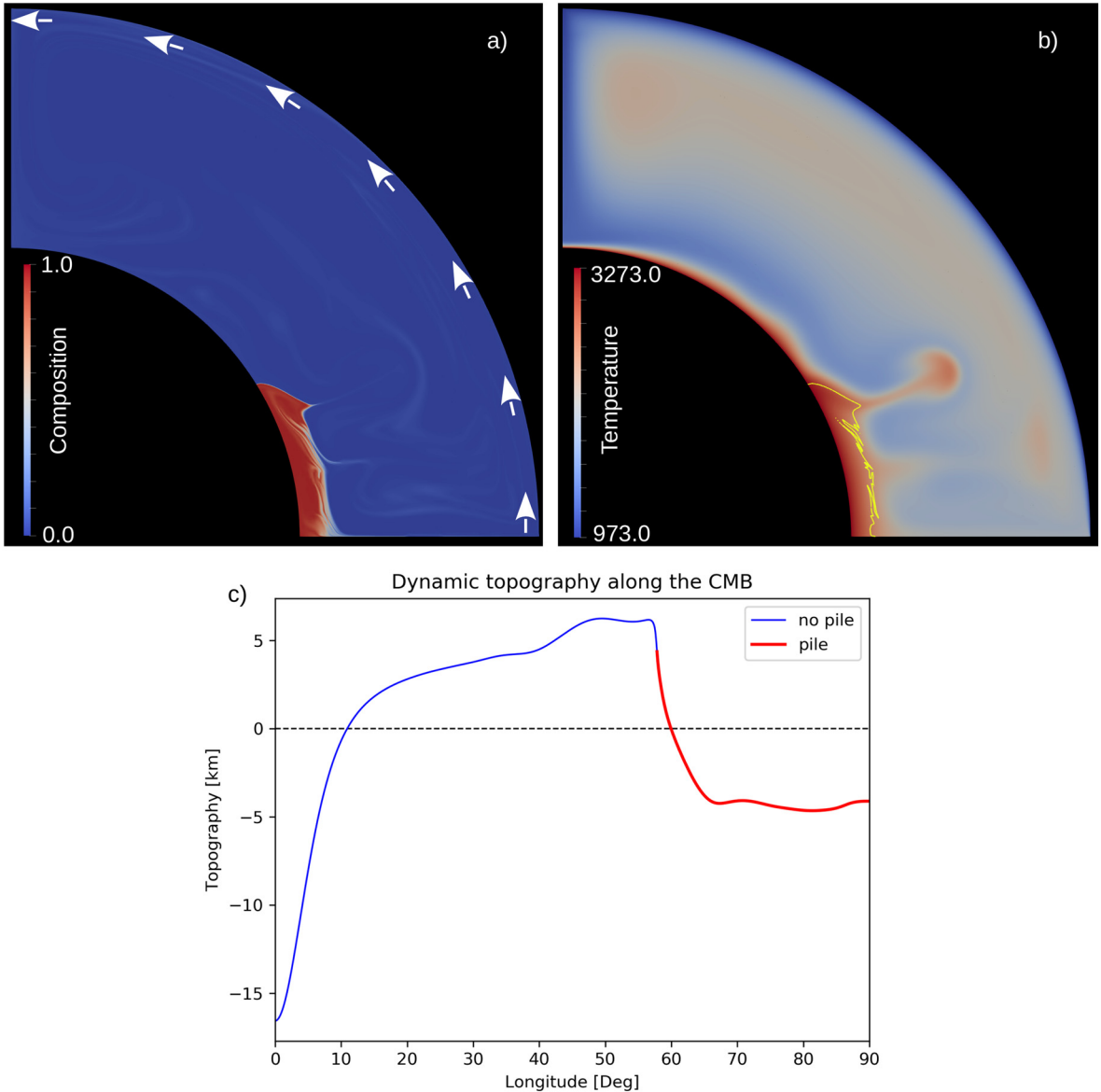


Fig. 2. Initial condition of (a) the compositional field and (b) the temperature field. White arrows in (a) indicate the velocity boundary condition, while the yellow line in (b) marks the outline of the pile for a composition value of $C = 0.8$. The general pattern of core-mantle boundary topography obtained for this type of model is shown in (c), with the line color indicating the area underneath the pile (red) and outside the pile (blue). Depressions are observed beneath the slab at 0° longitude due to the sinking flow, and beneath the dense pile. The area around the pile margin is uplifted due to rising flow. Topographic amplitudes, especially the depth of depression beneath the downwelling, strongly depend on the slab viscosity and might therefore be overestimated (see discussion in section 6.2), while the overall topographic patterns should be robust.

ferences therein), potentially making CMB topography even more important. Furthermore, it has been suggested that CMB topography affects convective flow in the outer core, thereby causing secular variations in Earth's magnetic field (Roberts and Aurnou, 2012).

There are several estimates of CMB topography derived from seismology (e.g., Tanaka, 2010; Koelemeijer et al., 2012; Schlaphorst et al., 2015; Colombi et al., 2014) and various geodynamic studies (Lassak et al., 2007; Steinberger and Holme, 2008; Yoshida, 2008; Lassak et al., 2010; Soldati et al., 2012; Deschamps et al., 2017; Deschamps and Li, 2019). Global maps of CMB topography up to spherical harmonic degree 4 can be obtained with normal modes (Koelemeijer et al., 2012) or body wave data (e.g., Tanaka, 2010), but both amplitudes and patterns of topography vary significantly between different studies due to trade-offs between CMB topography and the mantle's density and velocity structure (see e.g. Tanaka, 2010, and references therein). Geodynamic studies have

shown that low spherical harmonic degrees cannot distinguish between positive buoyancy-related topography generated by thermal plume clusters or thermochemical LLSVPs with less than 1.5% intrinsic density excess, whereas piles with excess density higher than 1.8–2% cause a depression of the CMB (Lassak et al., 2007; Steinberger and Holme, 2008; Yoshida, 2008; Lassak et al., 2010; Deschamps et al., 2017; Deschamps and Li, 2019). In addition, there are a few regional studies that use core-reflected waves for structures with wavelengths around 100 km (e.g., Restivo and Helffrich, 2006; Wu et al., 2014; Gassner et al., 2015; Schlaphorst et al., 2015; Mancinelli and Shearer, 2016; Shen et al., 2016). More recently, Mancinelli and Shearer (2016) obtained topography of even shorter length scales of approximately 7 km by analysing scattered energy. Yet, since observations of short-wavelength CMB topography are sparse, no systematic pattern of structures smaller than about 300 km has been detected yet.

In this study, we present numerical models to predict short-wavelength topography, showing that topographic length scales of about 100 km are sensitive to a potential viscosity contrast between thermochemical piles and the ambient mantle. Thus, measurements of short-wavelength topography at the CMB may constrain the thermal or thermochemical nature of LLSVPs. Moreover, it may allow for the identification of plumes at early stages.

2. Model setup

Our numerical models are run with the finite element code ASPECT (Kronbichler et al., 2012; Heister et al., 2017; He et al., 2017; Bangerth et al., 2018, 2019; Liu and King, 2019) in a 2-D spherical geometry. Equations describing the conservation of mass, energy and momentum are solved under the Boussinesq approximation. In general, the setup is similar to Heyn et al. (2018), and parameters are chosen so that the reference Rayleigh number, describing the vigor of convection via the definition

$$Ra = \frac{\alpha \rho g \Delta T d^3}{\kappa \eta}, \quad (1)$$

is equal to 10^7 . Parameters in equation (1) are thermal expansivity α , density ρ , temperature drop across the mantle ΔT , gravitational acceleration g , mantle thickness d , reference viscosity η and thermal diffusivity κ . Our domain is chosen as a quarter of an annulus along the equator with a grid that is adaptively refined based on the compositional and viscosity gradients after every 10 time steps of the calculation. Moreover, we performed runs for which cells are additionally refined in the lowermost mantle close to the core-mantle boundary, such that the CMB is sampled equally everywhere. The effective resolution in regular models varies between about 7×11 km and 80×90 km (lateral x radial), while our resolution tests have smallest cells of about 1.4 km at the CMB (see discussion further down). A constant uniform velocity boundary condition of 1.48 cm/year is imposed on the surface to force a single-plate degree-2 flow structure (Fig. 2a, comparable to observations from seismic tomography as shown in Fig. 1), while all other boundaries are free-slip. All parameters characterizing the general setup are given in Table 1.

Core-mantle boundary topography is derived from radial stresses calculated along the interface between mantle and core as benchmarked for ASPECT by Liu and King (2019) via the relation

$$h = \frac{\sigma_{rr}}{g \Delta \rho_{CMB}}, \quad (2)$$

with h being the CMB topography, σ_{rr} the radial component of the stress, and $\Delta \rho_{CMB}$ the density difference between core and ambient mantle, which is set to 4400 kg m^{-3} based on PREM (Dziewonski and Anderson, 1981). To ensure that our imposed plate velocity does not affect the core-mantle boundary topography, we also performed tests in which we replaced the surface velocity boundary condition by a free slip condition after a while. Since we have no slab-weakening mechanism, subduction in these models slowed down and finally stopped completely, thereby changing the mode of convection. However, during the transition phase, the observed dynamic topography does not change significantly until subduction stops, and the lateral thermal boundary layer (TBL) flow towards the pile ceases. Thus, we conclude that our choice of imposed surface velocity boundary condition does not affect the predicted CMB topography.

Our system is heated from below and from within by uniform internal heating (Table 1). Piles of dense material are represented by a compositional field that is advected with the discontinuous

Table 1

Characteristic parameters used in our thermochemical calculations. We convert excess densities into B (equation (3)) by assuming a 3300 K temperature drop across the mantle, which includes both the 2300 K superadiabatic temperature drop that we have in our models with the Boussinesq approximation, and an adiabatic temperature increase of 1000 K. Furthermore, although we assume a constant value of $\alpha = 3.0 \cdot 10^{-5}$ for the whole mantle within the models, we use a more realistic CMB thermal expansivity of $\alpha = 1.0 \cdot 10^{-5}$ at the CMB for conversion to B (Tackley, 2012). Based on that, we obtain buoyancy numbers comparable to previous studies (e.g., McNamara and Zhong, 2004; Mulyukova et al., 2015; Heyn et al., 2018). We also use the full temperature drop of 3300 K to calculate Ra , which is set to 10^7 . Within ASPECT, we use thermal conductivity k and specific heat capacity c_p instead of the thermal diffusivity κ , but they can be converted via $\kappa = \frac{k}{\rho c_p}$. In our models, we set κ equal to $1.0 \cdot 10^{-6} \text{ [m}^2/\text{s]}$.

Parameter	Symbol	Value [Unit]
Gravitational acceleration	g	$9.81 \text{ [m/s}^2]$
Mantle thickness	d	2890 [km]
Reference density (upper mantle)	ρ	$3340 \text{ [kg/m}^3]$
Reference viscosity	η	$7.83 \cdot 10^{21} \text{ [Pa}\cdot\text{s]}$
Thermal conductivity	k	$4.01 \text{ [W/K}\cdot\text{m]}$
Specific heat	c_p	$1200 \text{ [kg}\cdot\text{m}^2/(\text{K}\cdot\text{s}^2)}$
Thermal expansivity	α	$3.0 \cdot 10^{-5} \text{ [1/K]}$
Chemical excess density	$\Delta \rho_c$	$198.396 - 330.66 \text{ [kg/m}^3]$
Buoyancy ratio (eq. (3))	B	$0.6 - 1.0 \text{ []}$
Rayleigh number	Ra	10^7 []
Internal heating rate	H	$9.46 \cdot 10^{-13} \text{ [W/kg]}$
Imposed surface velocity	v_{surf}	1.48 [cm/yr]
Compositional viscosity contrast	η_c	$1 - 20 \text{ []}$
Thermal viscosity contrast	$\eta_{\Delta T}$	$2.3 - 7500 \text{ []}$
Temperature drop across mantle	ΔT	2300 [K]
Density difference core-to-mantle	$\Delta \rho_{CM}$	$4400 \text{ [kg/m}^3]$

Table 2

Parameters defining the viscosity profiles for different thermal viscosity contrasts $\eta_{\Delta T}$. We use steps at depths of 299 km, 410 km, and 660 km for the activation energy E_η , the temperature offset T_η , and the viscosity prefactor η_0 . In the table, values are sorted by increasing depth.

$\eta_{\Delta T}$	η_0	E_η	T_η
2.3	5	0.5 2.5 5 1 1 1 1	0.02 0.4 0.6 0.7
330	5	0.5 2.5 5 1 1 1 1	0.02 0.15 0.15 0.15
1700	5	0.5 2.5 5 1 1 1 1	0.02 0.12 0.12 0.12
7500	5	0.5 2.5 5 1.2 1.2 1.2 1.2	0.02 0.12 0.12 0.12

Galerkin method (He et al., 2017). A density contrast between thermochemical piles and regular mantle is prescribed via the buoyancy ratio

$$B = \frac{\Delta \rho_c}{\alpha \rho \Delta T}, \quad (3)$$

with $\Delta \rho_c$ being the density difference due to composition.

Similar to Heyn et al. (2018), our viscosity depends on temperature, depth and composition, given by

$$\begin{aligned} \eta(z, T, C) &= \eta_0(z) \eta_{\Delta T}(z, T) \exp[C \ln \eta_C] \\ &= \eta_0(z) \exp \left[\frac{E_\eta(z)}{T^* + T_\eta(z)} - \frac{E_\eta(z)}{1 + T_\eta(z)} + C \ln \eta_C \right] \end{aligned} \quad (4)$$

with the non-dimensionalised temperature T^* , that is cut off between values of 0 and 1. Non-dimensionalisation is done using the reference values of $T^* = 0$ and $T^* = 1$ for the surface and the CMB temperature, respectively. The dependence on depth is implemented as steps of the viscosity prefactor η_0 , the non-dimensional activation energy E_η and the non-dimensional temperature offset T_η (Table 2). η_C is the temperature-independent intrinsic viscosity contrast between the pile and the ambient mantle due to composition, varying between 1 and 100, while C is the composition value between 0 and 1. $\eta_{\Delta T}$ is the thermal viscosity contrast and describes the maximum potential viscosity variations due to temperature in the lower mantle, which we vary in the range 2.3 to

Table 3

Overview of the models we analysed in this study. For each combination of B and $\eta_{\Delta T}$ indicated by +, we used the values $\eta_C = 1, 2, 3, 5, 8, 10, 15, 20, 50$ and 100, while combinations marked with – have not been tested.

B	$\eta_{\Delta T}$	2.3	330	1700	7500
0.6	–	+	–	–	–
0.8	+	+	+	+	–
1.0	–	+	–	–	–

7500. These values are at the lower end of the range often used in geodynamic studies (e.g., Li et al., 2014), but may be consistent with geoid constraints (Yang and Gurnis, 2016). All combinations of B , $\eta_{\Delta T}$ and η_C used in this study are listed in Table 3.

To achieve a better comparison between parameters and to avoid highly variable topography during pile formation, all models begin from the same reference case of a fully-developed system with degree-2 structure (see Figs. 2a and 2b). We obtain this initial condition by running a model with the reference values of $B = 0.8$, $\eta_{\Delta T} = 330$ and $\eta_C = 6$ for 6.5 Gyr, starting with a 125 km thick dense basal layer (as described in Heyn et al. (2018)). This results in a pile with a volume of about 1.75% of the mantle (approximately 77% of the original layer mass, Fig. 2b), and removes topographic variations due to different initial pile masses. Although such a setup means that models require some time to adjust to the changed parameters, the uniform mass and volume of the initial condition enables us to expand our investigation of the effects of density and viscosity towards pile configurations that would be unstable otherwise. To overcome the limitation of adjustment time and to get better constraints on how topography changes when plumes interact with the pile, we run our models for 2.5 Gyr. Since this study is focussed on the investigation of short-wavelength topographic patterns for present-day lower mantle structure (Fig. 1), neither pile formation processes nor the potentially overestimated absolute amplitudes of CMB topography in Fig. 2c are significant, as discussed in section 6.2.

3. Characteristic topography for higher intrinsic pile viscosity

For models without an elevated intrinsic pile viscosity, the CMB topography shows depressions beneath the subducting slab and beneath the dense pile, while the CMB at the pile margin is uplifted and shows strong positive topography (Fig. 2c). This reflects the general flow pattern of sinking flow beneath the slab and rising hot flow at the pile margin, with isostatic adjustment for the dense pile itself. Relative (and also absolute) topography amplitudes depend on the thermal viscosity contrast $\eta_{\Delta T}$, since increasing the temperature-dependence of viscosity makes slabs stronger and thus increases the coupling between mantle flow and the CMB. As a consequence, the depression beneath the slab gets more pronounced with increasing $\eta_{\Delta T}$, while the pile depression gets smaller. The latter is, however, more likely related to pile thickness and density than it is to viscosity (as discussed later in more detail). Increasing the pile excess density (B) or the pile viscosity (η_C) increases the pile depression, while topography beneath the slab is not affected. These observations are in good agreement with previous studies (Lassak et al., 2007, 2010; Deschamps et al., 2017) and also fit the pattern of long-wavelength CMB topography detected by body waves or normal modes reasonably well (Tanaka, 2010; Soldati et al., 2012).

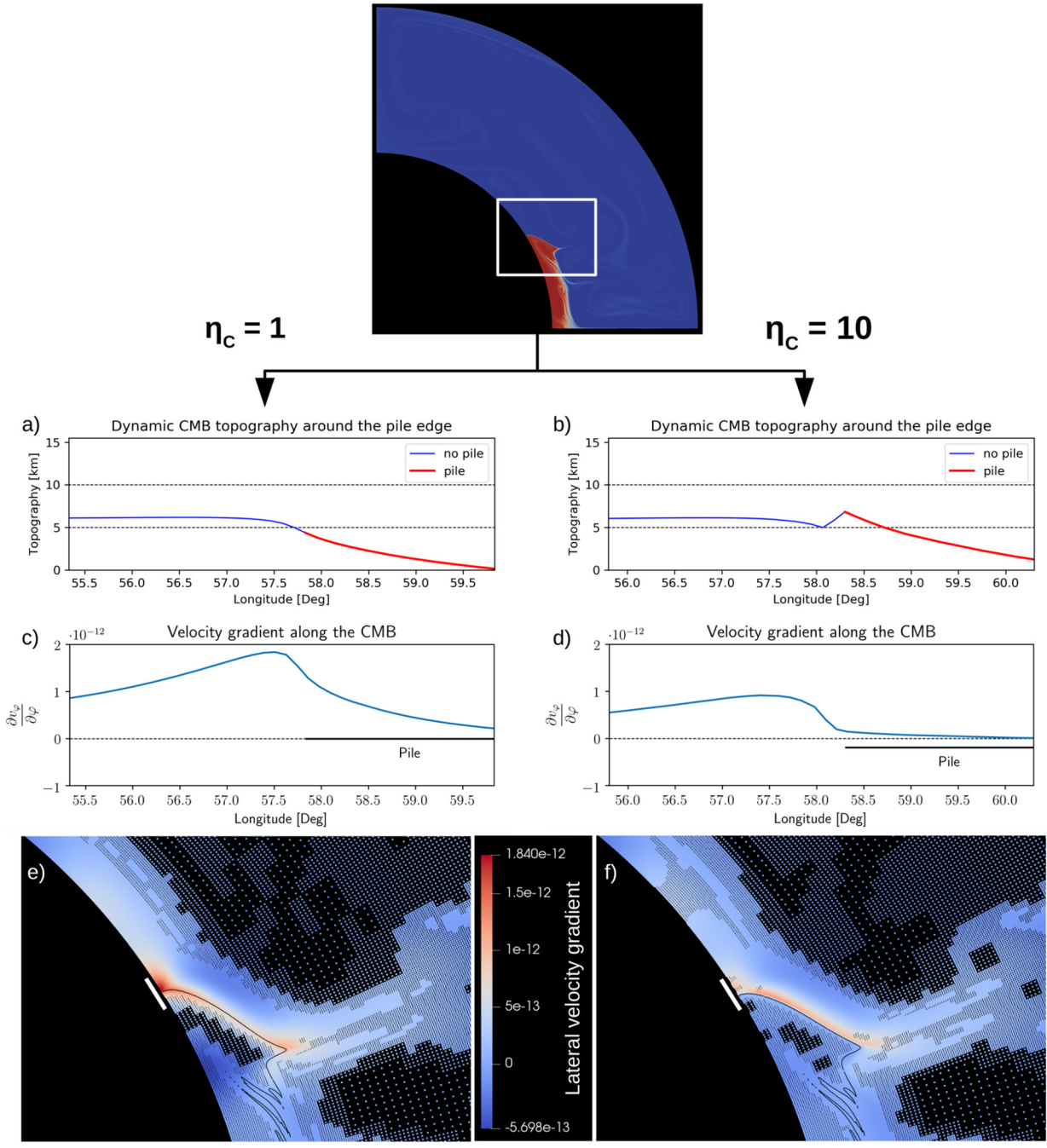
Although the long-wavelength pattern of topography is not significantly affected by the presence of a compositional viscosity contrast (in good agreement with Deschamps et al. (2017)), we observe strong differences at shorter length scales. Fig. 3 compares the topography for a model with $B = 0.8$, $\eta_{\Delta T} = 330$ and $\eta_C = 1$ (Fig. 3a, left panels) with $\eta_C = 10$ (Fig. 3b, right panels),

the former being the same parameters as for the representative long-wavelength topography in Fig. 2c. Yet, as can be seen in the topographic profile in Fig. 3 (right), the core-mantle boundary shows a clear depression next to the pile edge that is approximately 80–120 km wide (measured from the top of the plateau outside the pile to the maximum beneath the pile edge, 1° corresponds to 61 km at the CMB) and a peak that marks the edge itself. We observe these features only if the pile has a higher intrinsic viscosity than the surrounding hot thermal boundary layer, otherwise the topography near the pile margin is smooth. The amplitude of the depression (about 2–3 km) is smaller than that of the long-wavelength elevation associated with rising flow at the pile margin (compare the elevation at 40–60° longitude in Fig. 2c). Consequently, the overall topography remains positive and the depression is not visible at low spherical harmonic degrees. Neither long-wavelength nor short-wavelength topography are changed significantly within our resolution tests (compare Figs. 3g and 3h with 1.4 km resolution to Figs. 3a and 3b with 7 km resolution), only the amplitudes of the small-scale topographic feature and its symmetry are slightly modified as we capture their slopes more accurately.

A reduced density of hot TBL material and uplift due to rising flow explain the long-wavelength topographic high near the pile, and thus also the local peaks of the short-wavelength topography. For more viscous (stiffer) piles, the uplift of the CMB is asymmetric and more pronounced beneath the pile margin due to increased coupling between the mantle and the CMB. However, the origin of the small-scale depression outside the pile margin can only be partially explained by the relative uplift of the pile margin, and is not related to density differences in the lower mantle, since the material from which plumes are sourced is hot and therefore light. Yet, the distribution of lateral gradients for the velocity component parallel to the CMB ($\frac{\partial v_\phi}{\partial \varphi}$) changes significantly in the presence of a stiff pile with $\eta_C > 1$ (compare Figs. 3c–f). While the gradient is distributed over a broad area with its maximum about 0.3 degree from the pile edge in the case of $\eta_C = 1$ (Fig. 3c), a higher pile viscosity $\eta_C = 10$ focusses the stress in a localized area just outside the pile margin, with hardly any velocity gradient within the pile itself (Fig. 3d). Consequently, compression associated with velocity gradients in lateral TBL flow becomes concentrated in a narrow area outside a high-viscosity pile, causing radial stress towards the CMB, expressed as a depression.

4. How small-scale topography relates to the plume cycle

Since short-wavelength CMB topography is related to flow compression at the pile margin, it is strongly time-dependent and changes according to the positions of plumes and the dynamics of piles. In order to relate observations obtained with seismology to the dynamics of plume interactions with the LLSVPs, we need to understand how the CMB topography changes with time during the formation of plumes. Fig. 4 shows the evolution of several topographic characteristics for the models discussed above as a function of time (left: $B = 0.8$, $\eta_{\Delta T} = 330$ and $\eta_C = 1$, right: $B = 0.8$, $\eta_{\Delta T} = 330$ and $\eta_C = 10$). These are: (1) the maximum slab depression, (2) the average pile depression, excluding elevated parts of the CMB beneath the pile, (3) the highest point outside the pile, i.e. the “plume-side plateau” (PSP), (4) the lowest point next to the pile, i.e. the “circum-pile depression” (CPD), and (5) the highest point inside the pile, i.e. the “pile-edge maximum” (PEM). In case of $\eta_C = 1$, points (4) and (5) occur at adjacent nodes of the mesh, thus the topographic difference between the two is mesh-dependent. As can be seen, the maximum slab depression does not change much with time, while the three points defining the short-wavelength depression show a quasi-periodic behaviour, although slightly shifted in time for piles with increased intrinsic viscosity.



Resolution test:

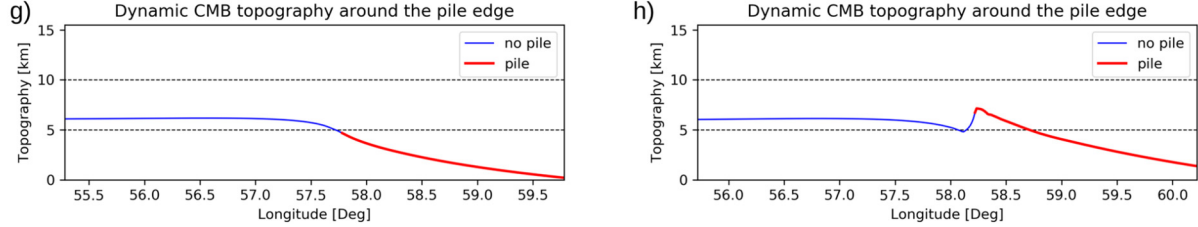


Fig. 3. CMB topography near the pile edge (panels (a), (b)) and its associated lateral velocity gradient (panels (c)-(f)) for models with $B = 0.8$, $\eta_{\Delta T} = 330$ and $\eta_c = 1$ (left) or $\eta_c = 10$ (right). The position and length of the profiles are indicated by white lines in (e) and (f). As can be seen in (b), there is a characteristic short-wavelength topography related to an increased pile viscosity. This topographic pattern is observed for all values of $\eta_c > 1$, although depth of the depression and the peak at the pile margin increase with pile viscosity. The depression is caused both by a relative uplift of the pile-edge maximum (compared to the plume-side plateau, see definitions in Fig. 4), and a wedge of TBL material that gets compressed against the pile. The latter results from the lateral gradients of the velocity component parallel to the CMB ($\frac{\partial v_\varphi}{\partial \varphi}$) shown in (c) and (d) along the CMB, and in (e) and (f) as points at cell centres. While the gradient in the left panel (case $\eta_c = 1$) spreads into the pile, a stiffer pile exhibits almost no velocity gradient. The lowermost row shows the topography obtained for the same set of parameters, but uses a resolution of up to 1.4 km to verify that the observed topography is not an artifact of resolution. Apart from details of the slopes, there is no change in topography for our resolution test.

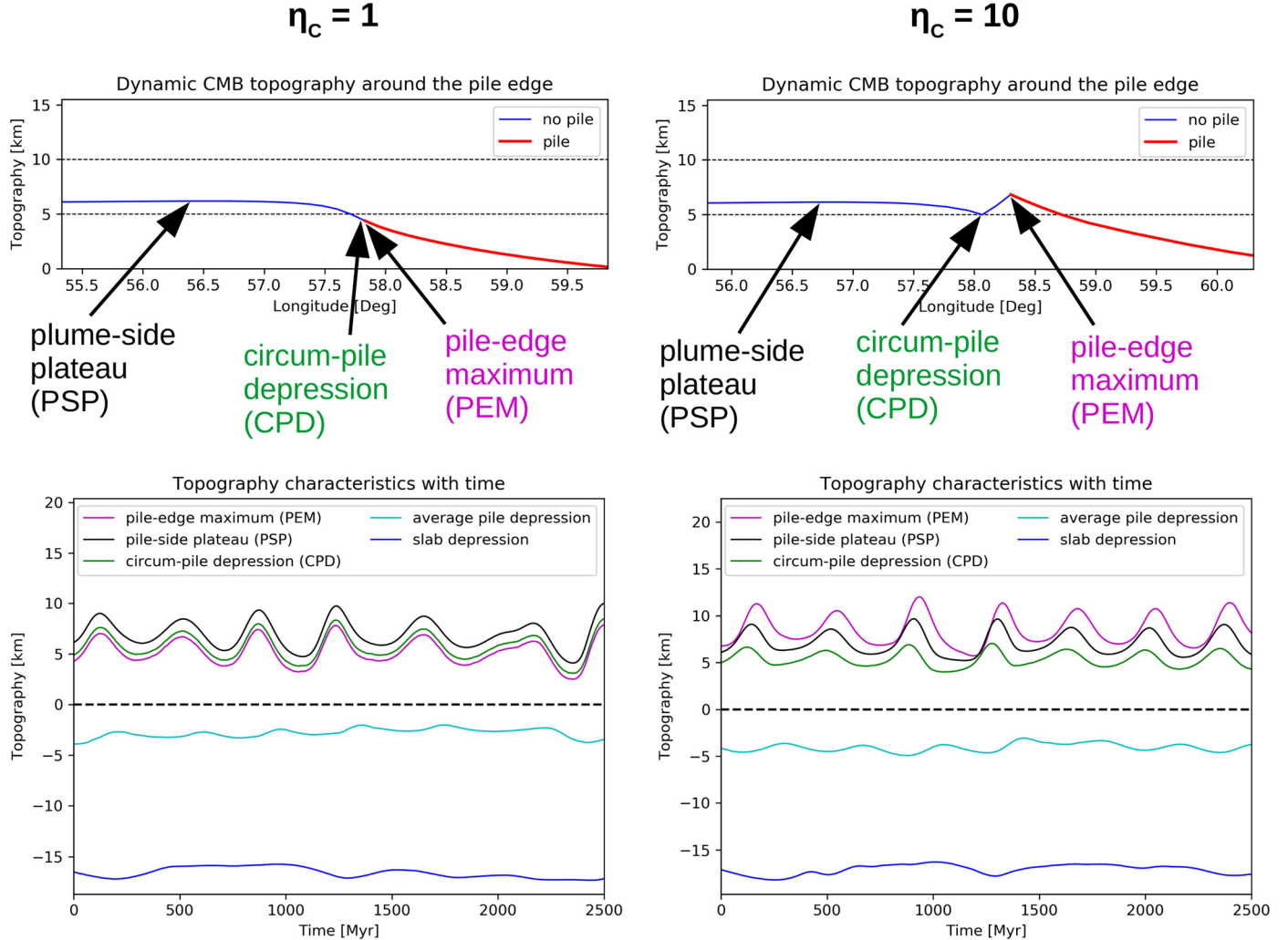


Fig. 4. CMB topography characteristics and their evolution over time for the models discussed in Fig. 3: $B = 0.8$, $\eta_{\Delta T} = 330$, $\eta_c = 1$ (left), and $B = 0.8$, $\eta_{\Delta T} = 330$, $\eta_c = 10$ (right). Note that in the case of $\eta_c = 1$ (left), there is no depression or pile-edge maximum, thus these points mark the lowest topography just outside the pile and the maximum topography inside the pile, which are adjacent gridpoints. Slab depression is the maximum depression beneath the subducted slab (usually at longitude 0) and the average pile depression describes the average of the negative CMB topography beneath the pile. The periodic behaviour of the topography characteristics near the pile edge is caused by the initiation of plumes and their interaction with the pile.

This reflects the periodic generation of plumes at the pile margin (Heyn et al., 2020), which is caused by a local collapse of the thickened pile edge associated with a reduction of plume pull for fading or laterally moving plumes (Fig. 5). This pile collapse is also reflected in the periodicity of the average pile depression, which shows a minimum approximately every time the pile collapses, although the amplitudes are rather small compared to variations at the pile margin (Fig. 4).

An example of how the topography around the pile margin and its associated velocity gradient evolve during a plume cycle is shown in Fig. 5. For each step, the figure is divided into the topography around the pile edge and the lateral gradient of v_ϕ (the velocity component along the CMB). Velocity gradients are calculated at the cell centres of the respective mesh and are represented as points, thus also indicating the actual mesh resolution. As mesh resolution is refined based on gradients in composition and viscosity, it allows us to identify the pile outlines and the plumes. For orientation, the outline of the pile is also indicated as black line in the velocity gradient field. When comparing the velocity gradients over time, we can clearly see that their magnitude varies significantly, while the sign is preserved throughout the whole cycle.

When a plume rises at the pile margin (Fig. 5a), it drags material towards the pile while compressing the pile laterally and lo-

cally increasing the pile thickness. Yet, since the stiffer pile moves much slower than the hot ambient mantle, we get a velocity gradient and thus compression at the pile edge. Part of this compressed ambient mantle material can escape upwards in the plume, but we are left with a wedge of hot mantle that is trapped against the steep pile edge. When the plume moves towards the top of the pile (Figs. 5b-c), it exerts less drag on the hot thermal boundary layer, while the pile edge moves along the CMB in the same direction as the lateral TBL flow, and pile area is reduced. This reduces the velocity gradient, and the topographic depression becomes less pronounced. The gradient is then a minimum at the time when the pile edge reaches its maximum thickness and the lateral motion of the pile margin ceases (Fig. 5c, see also Heyn et al. (2020)). At this time, the plume has lost its connection to the thermal boundary layer, and the velocity towards the pile within the TBL decreases. The smaller velocity gradient is also reflected in the topographic depression of the CMB next to the pile, which reaches a minimum in amplitude, while the adjacent topographic maxima become more symmetric.

As the pile collapses and expands along the CMB (Figs. 5d-e), it pushes the hot TBL material against the prevailing flow along the CMB towards the pile, induced by the sinking slab, and considerably increases the velocity gradient just outside the stiff pile

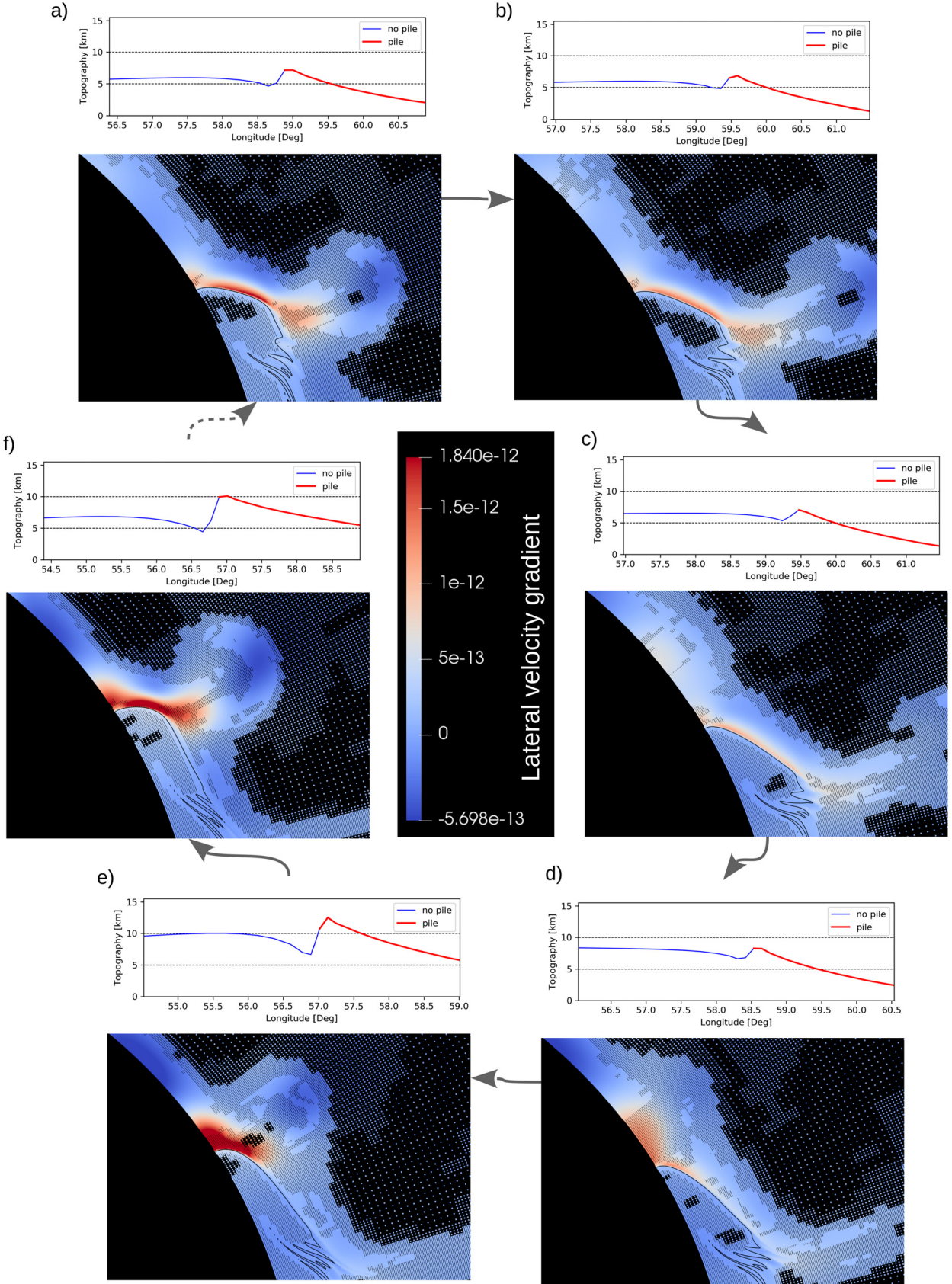


Fig. 5. CMB topography and lateral velocity gradients of v_φ during a cycle of plume initiation and growth. A plume being pushed towards the pile interior increases the local pile edge thickness, while pulling the pile margin along the TBL in the flow direction, thereby reducing the lateral velocity gradient and the topographic depression (panels (a)-(c)). As soon as the upward plume pull decreases and no longer supports the thickened pile, the pile edge starts to collapse and spread along the CMB in a direction opposite to the TBL flow (panels (c) to (e)). This increases compression in the TBL wedge significantly, which amplifies CMB topography. It also thickens the lower thermal boundary layer, triggering a new plume (e). When the plume starts to rise, the lateral pile edge motion stops, the velocity gradients and CMB topography start to decrease (f), and the cycle starts anew.

(Fig. 5d). As long as the plume is not fully developed (Fig. 5e), only a small portion of the compressed material can escape upwards, and a large and asymmetric depression develops outside the pile. As soon as the plume starts to rise (Fig. 5f), the lateral pile edge motion comes to a halt and the compression becomes weaker. The cycle repeats itself for every plume, and since both the symmetry and amplitude of the circum-pile depression vary along this cycle, they might be used as indicators for the current stage of the plume cycle.

5. The effect of varying density and viscosity contrasts

For long wavelengths, our predicted dynamic CMB topography, and its principal dependence on the viscosity structure of the lower mantle and the density of the pile, agree well with previous studies (e.g., Lassak et al., 2007, 2010; Deschamps et al., 2017). Yet, since a higher value of $\eta_{\Delta T}$ in our models does not reduce the TBL viscosity (equation (4)), the elevation of the CMB associated with rising flow is not reduced either. The implications of this are discussed later.

In the following section, we focus on the characteristic short-wavelength topography at pile margins. Since this CMB topography is superimposed on the long-wavelength component, we use relative topography between the three characteristic points (Fig. 4) to describe our observations as a function of pile and TBL properties. Apart from determining whether there is a valley-shaped circum-pile depression or not, the lowermost mantle viscosity structure and pile density are expected to have different effects on the depth and symmetry of the characteristic topography, since they influence different parts of the topographic pattern. Thus, observations of this topography (e.g., from seismology) could place useful constraints on these viscosity variations.

5.1. Time-averaged topography

The compositional viscosity contrast η_C has a strong impact on relative topography, both in terms of the depth of the depression and the asymmetry of the peaks. Especially for $\eta_C < 30$, the depression and the peaks become more pronounced (Figs. 6a-d) and asymmetric (Figs. 6e-f) with increasing η_C . The latter can be explained by increased coupling between the stiff pile and the CMB for larger values of η_C (Lassak et al., 2007, 2010; Deschamps et al., 2017). In contrast, the increased relative topography between the plume-side plateau (PSP) and the depression (CPD) in Figs. 6c-d occurs because stiffer piles focus more of the lateral velocity gradient into the compressed TBL wedge, thus increasing the stresses there. Relative topography values close to zero in Figs. 6a-b or negative values in Figs. 6e-f show the absence of characteristic short-wavelength topography for piles that are not more viscous than their surroundings. By contrast, the plume-side plateau is always more elevated than the “depression” due to our definition (Fig. 4 left panels).

The effect of thermal viscosity contrasts is a bit more ambiguous than that of η_C . As can be seen in Fig. 6 (left), increased temperature-dependence $\eta_{\Delta T}$ (indicated by line color) reduces the depth of the depression relative to both peaks (Figs. 6a and 6c), and makes the structure more symmetric by reducing the elevation difference between the two topographic maxima (Fig. 6e). Yet, changes are minor compared to the influence of the pile viscosity (η_C , x-axis). The observed decrease in relative topography between the characteristic points of the short-wavelength topography is related to an increase in plume strength caused by fewer plumes forming in a given time period for increasing $\eta_{\Delta T}$. Less frequent plume formation gives the lower thermal boundary layer more time to grow and results in stronger plumes. This effect is

most pronounced outside the pile (plume-side plateau and depression) because stronger plumes also increase the pile edge thickness more, partly compensating the increased upward pull (via isostatic compensation). Increased lateral viscosity variations above the TBL for larger values of $\eta_{\Delta T}$ are not important for CMB topography.

Increasing the pile density generally reduces the elevation of the CMB beneath the pile. This is expressed in the reduced relative topography between the pile-edge maximum and the plume-side plateau (Fig. 6f), making the characteristic topography more symmetric. Yet, the difference between the pile-edge maximum and the depression (Fig. 6b) is hardly affected, indicating that the depression must become deeper (which it does relative to the plume-side plateau, see Fig. 6d). Thus, a denser pile focusses stresses in a wedge of TBL material next to the pile margin, similar to the effect of η_C , although significantly smaller in amplitude.

5.2. Topography variations during the plume cycle

As shown in Fig. 5, the symmetry and depth of the characteristic depression vary significantly during the plume cycle in response to plume initiation and pile collapse (Heyn et al., 2020). Similar to the time-averaged topography discussed above, these variations in symmetry and depth depend on B , η_C and $\eta_{\Delta T}$ (Fig. 7), and may thus give additional constraints on the structure of the lowermost mantle. In order to quantify these, we calculate the minima and maxima of relative topography within each cycle of initiation and fading of plumes, and average the obtained values by the number of observed plume cycles. However, the maxima and minima of relative topography do not necessarily occur at the same time within the plume cycle, but may be slightly delayed relative to each other (compare Fig. 4).

As can be seen, neither the thermal viscosity contrast (Fig. 7a) nor the pile density (Fig. 7b) have any significant impact on the minima and maxima of relative topography during the plume cycle. Increasing B or $\eta_{\Delta T}$ reduces the amplitude of topography variations slightly. For $\eta_{\Delta T}$, this reflects the effect of increased plume strength, which is more pronounced outside the dense pile, while an increased pile density B damps the motion of the pile-edge maximum. Since the plume-side plateau and the circum-pile depression are in both cases affected in the same way, the range of differential topography between these points is almost constant.

In contrast, increasing η_C , especially for $\eta_C < 30$, leads to significant increases in relative topographies, with the strongest increase observed for the relative topography between the pile-edge maximum and the circum-pile depression (Fig. 7c, PEM-CPD). This reflects the combined effects of increased focussing of stresses during the plume cycle (plume-side plateau vs depression, Fig. 7c, PSP-CPD), and a stronger vertical motion of the pile-edge maximum for stiffer piles (pile-edge maximum vs plume-side plateau, Fig. 7c, PEM-PSP). As a consequence, a stronger compositional viscosity contrast considerably increases the variations in depth and asymmetry of the characteristic short-wavelength topography, while pile density and thermal viscosity contrasts have negligible effects.

6. Discussion

6.1. Observations of CMB topography

Up to now, there have been few seismic observations of short-wavelength core-mantle boundary topography, but the number of observations has been increasing in recent years due to improvements in equipment and methodology (Restivo and Helffrich, 2006; Wu et al., 2014; Gassner et al., 2015; Schlaphorst et al., 2015; Mancinelli and Shearer, 2016; Shen et al., 2016). Schlaphorst et

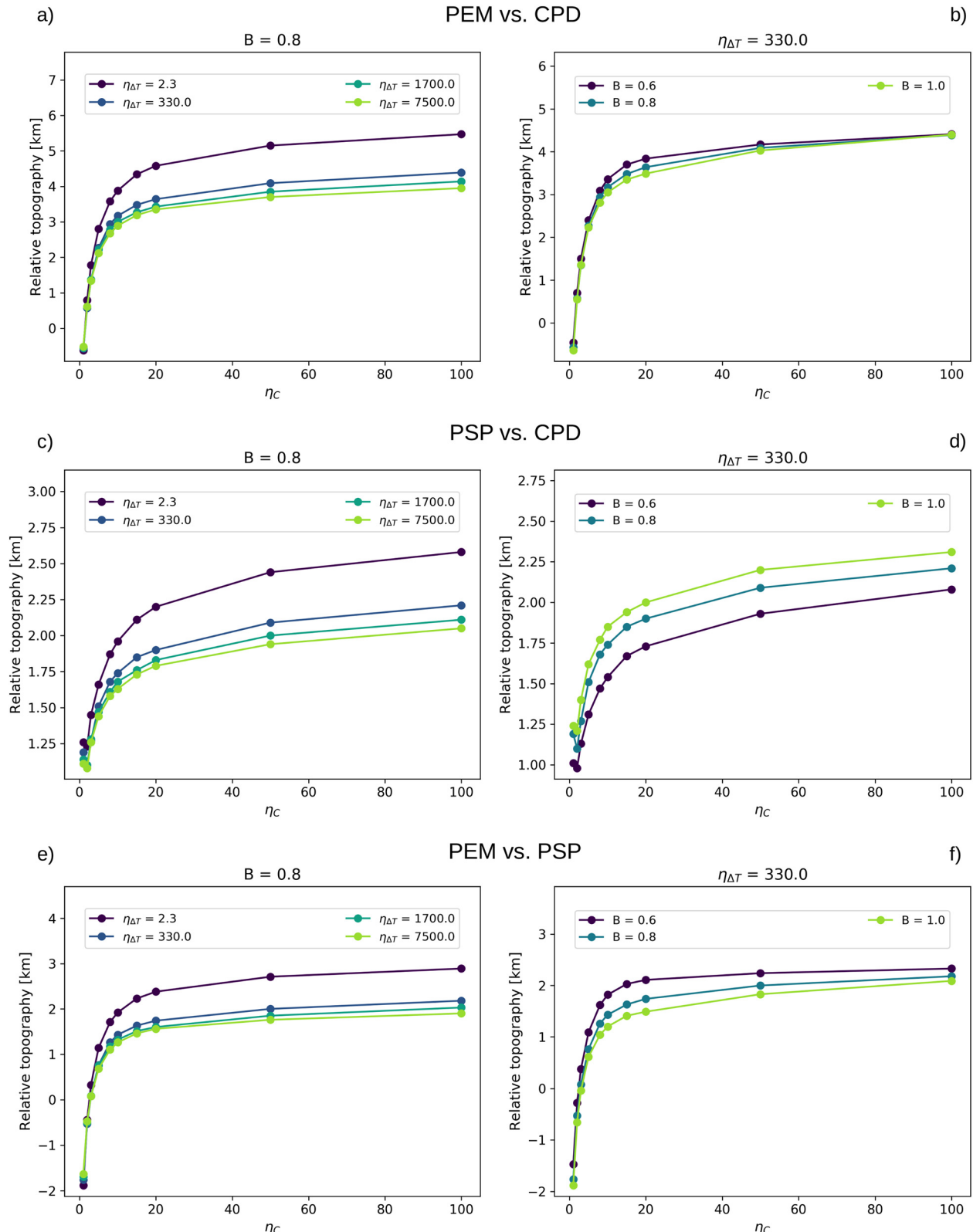


Fig. 6. Time-averaged relative topography between different points defining the characteristic topography at the pile margin as a function of η_c and $\eta_{\Delta T}$ for $B = 0.8$ (left) or as a function of η_c and B for $\eta_{\Delta T} = 330$ (right). Relative topographies between the pile-edge maximum (PEM) and the circum-pile depression (CPD) (a)-(b) and the two maxima (PEM and PSP) (e)-(f) increase with increasing η_c , while both $\eta_{\Delta T}$ and B play minor roles. Negative topography values indicate the absence of the depression (compare Fig. 4, left panels). The increase in relative topography between the plume-side plateau (PSP) and the circum-pile depression with increasing η_c (second row, panels (c)-(d)) reflects a stronger focussing of stresses into the compressed TBL wedge. Due to the definition of these characteristic points (Fig. 4), the relative topography never reaches zero. The data can be found in the Supporting Information, Table S1.

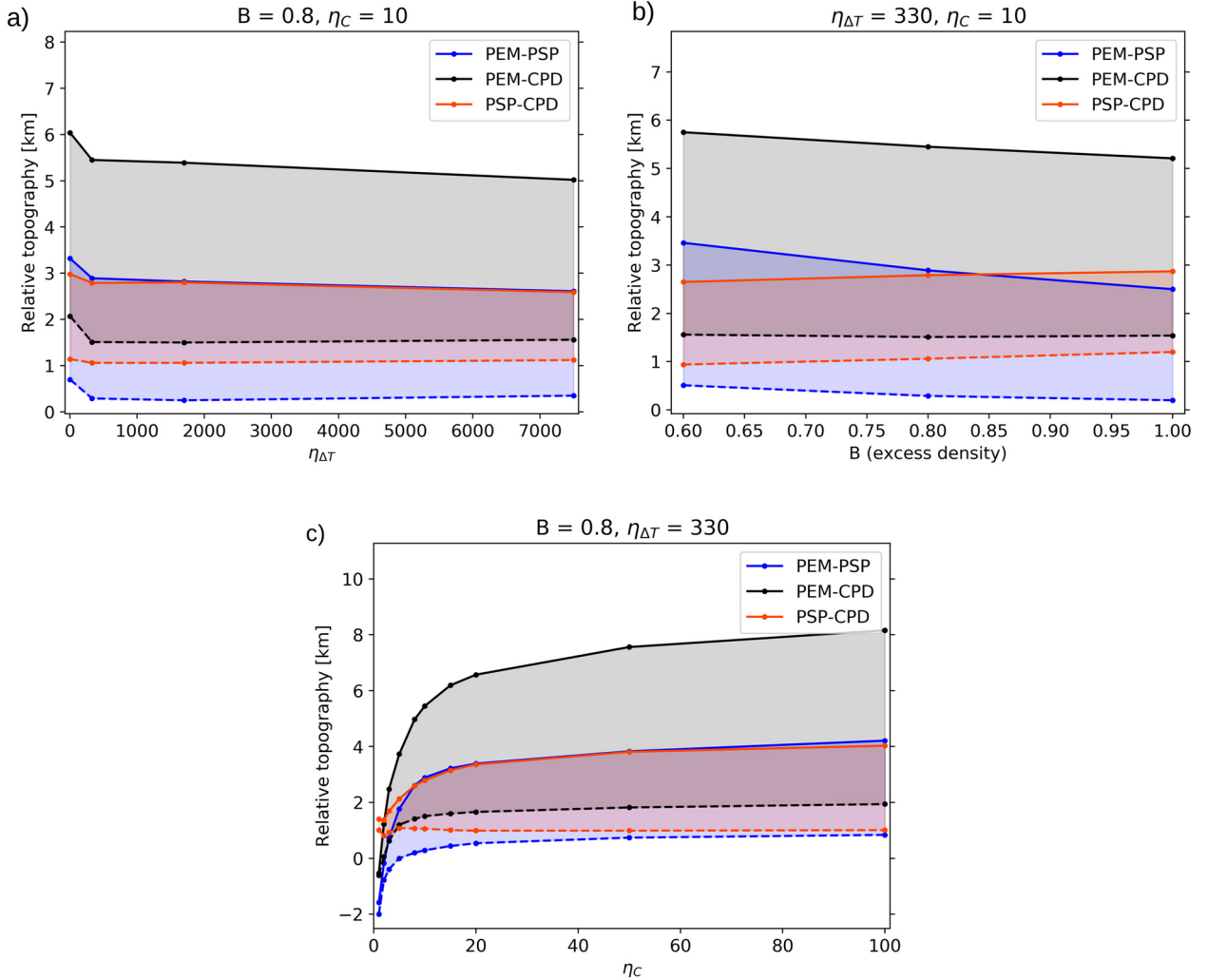


Fig. 7. Average variations of relative topography during the plume cycle as a function of the thermal viscosity contrast $\eta_{\Delta T}$ (a), the pile density B (b), and the compositional viscosity contrast η_C (c), while the other parameters are fixed as indicated. Abbreviations are: PSP = plume-side plateau, PEM = pile-edge maximum, and CPD = circum-pile depression. Colored dashed and solid lines indicate the average minima and maxima (respectively) of relative topography between the respective characteristic points during the plume cycle (see text for more details). The data can be found in the Supporting Information, Table S2.

al. (2015) give an overview of studies using body waves to investigate CMB topography, most of which investigate length scales of about 100–1000 km, and their resulting topography magnitudes. The shortage of observations of small-scale topography and the large variability in patterns and magnitudes of current CMB topography maps are caused by several factors: (1) the resolution of body waves and normal mode data limit most methods to topography length scales of > 100 km (Koelemeijer et al., 2012; Soldati et al., 2013; Schlaphorst et al., 2015), although there are a few studies that infer smaller wavelengths based on PKP and PKKP precursors (see e.g., Schlaphorst et al., 2015; Mancinelli and Shearer, 2016, and references therein); (2) there is a trade-off in normal mode or traveltimes data between topography and other parameters such as density above and below the CMB or the seismic velocity structure, which makes interpretation of data non-unique (Steinberger and Holme, 2008; Koelemeijer et al., 2012); (3) for core-reflected waves (e.g. P_cP and S_cP), which have a maximum resolution of about 100 km, both data processing, data quality and available source-receiver combinations limit the applications (Colombi et al., 2014; Wu et al., 2014; Shen et al., 2016). With the current methods, core diffracted waves, such as P_{diff} can be even more problematic and may not be useful to investigate CMB topography of short- to intermediate length scales (Colombi et al., 2014). As a consequence, we currently have only limited long-wavelength data (Tanaka, 2010;

Soldati et al., 2012) and a few regional studies (Wu et al., 2014; Gassner et al., 2015; Schlaphorst et al., 2015; Shen et al., 2016). Although there is no systematic study of CMB topography around or beneath the LLSVP structures to which we could compare our predictions, advances in seismic data coverage may provide the basis for a more detailed CMB topography in the future.

The length scale of approximately 80–120 km for our predicted topography is comparable to the maximum lateral resolution of about 100 km obtained for core-reflected waves, such as S_cP and P_cP (Wu et al., 2014; Schlaphorst et al., 2015; Shen et al., 2016). Yet, focussing or defocussing effects of CMB depressions or elevations on core-reflected waves may enable us to detect topography on even slightly smaller topographic length scales of about 60 km (Wu et al., 2014; Shen et al., 2016). By applying this method to Earth, Wu et al. (2014) and Shen et al. (2016) have detected topography with length scales between 140 and 350 km and amplitudes up to 6 km beneath Alaska and Japan. Moreover, Mancinelli and Shearer (2016) recently used scattered energy to infer globally random core-mantle boundary topography of about 400 m amplitude and lateral scales down to about 7 km, which would be sufficient to investigate structures of the length scales predicted by our models. However, data processing of this type of signal is still in its early stages, making a direct comparison to observations currently

unfeasible (Mancinelli and Shearer, 2016), but potentially possible in the future.

6.2. Model limitations

Taking into account differences in our viscosity law, our results for long-wavelength topography agree well with previous studies (Lassak et al., 2007, 2010; Deschamps et al., 2017; Deschamps and Li, 2019) with respect to the dependence of long-wavelength CMB topography on viscosity contrasts and density. However, in contrast to e.g. Deschamps et al. (2017), our viscosity law (Eq. (4)) results in the same viscosity of high-temperature plumes for all values of $\eta_{\Delta T}$. Thus, our viscosity law allows us to isolate the impact of plume strength on CMB topography, which is otherwise masked by the dominant effect of topography reduction due to lower plume viscosities. In our models, the change in thermal viscosity contrast has the strongest effect on the viscosity of cold material, and therefore has a tendency to overestimate the depth of long-wavelength depressions beneath the slabs, e.g. compared to Deschamps et al. (2017). Thus, we may over- or underestimate some amplitudes, while the background topographic pattern at long-wavelengths, and the structure and time-dependence of the short-wavelength topography, should be robust.

It has been shown that the presence of post-bridgmanite with a viscosity 3–4 orders of magnitude below that of bridgmanite (Ammann et al., 2010) can reduce the depression induced by the sinking slab considerably (Yoshida, 2008; Deschamps and Li, 2019). This effect may be necessary to make geodynamic predictions consistent with the CMB topography amplitudes inferred from seismology (Yoshida, 2008; Soldati et al., 2013), which vary between a few hundred meters and a few kilometers (e.g., Tanaka, 2010; Soldati et al., 2012; Wu et al., 2014; Schlaphorst et al., 2015). For the short-wavelength topography, the effect of weak post-bridgmanite should depend on its distribution. If post-bridgmanite is stable only in cold areas outside the LLSVPs, i.e. subducted slabs (Torsvik et al., 2016), our observed topographic pattern may become more asymmetric due to a viscosity decrease outside the pile and a stronger focussing of stresses into the TBL wedge. Such a scenario would correspond to an increase in the compositional viscosity contrast in our models. The potential presence of (basaltic) post-bridgmanitic thermochemical LLSVP piles might eliminate or greatly reduce compositional viscosity contrasts between piles and TBL material, causing reduced topography at pile margins. In the case of composite LLSVPs with a stable bridgemanitic base layer (about 200 km thick) with overlying less stable low-viscosity basaltic material (about 100 km thick), the basal layer would act as the high-viscosity pile that we investigated in most of the models here. The latter scenario has been suggested by Trønnes et al. (2019), based on available mineral physics data and seismic evidence for the post-bridgmanite distribution (Koelemeijer et al., 2018).

Our use of a uniform starting model with a fully-developed pile for all different combinations of parameters B , $\eta_{\Delta T}$ and η_C has several implications. As pointed out above, models need about 50–200 Myr to adjust to the modified condition, including changes in pile morphology (thickness and CMB area coverage) and the plume cycle. As a consequence, relative topography amplitudes adjust as well, while the general topographic pattern does not change during the adjustment time. Since we take averages over 2.5 Gyr, including several plume cycles with natural variations in themselves, this adjustment time does not significantly influence our conclusions. However, this kind of setup enables us to ignore the potential effect of a variable and rather unconstrained pile density and viscosity that we would get as an initial condition after pile formation with different parameters. Although certain combinations of low buoyancy number and small compositional viscosity

contrast may not lead to stable degree-2 piles when starting with a basal layer (e.g. Li et al., 2014; Heyn et al., 2018), these combinations may still be possible, although less likely, within Earth. Since stability of thermochemical piles also depends on the deformation history of the dense material, piles may be stable for an extended range of parameters if pile formation does not include a phase of strong deformation (see Heyn et al. (2018)). Another possibility is a reduction of the excess density and viscosity of stable piles after their formation via the entrainment of ambient mantle or recycled oceanic crust into the piles, both of which have lower density and viscosity than the bridgemanitic material we assume in this work. Although the general topographic pattern is not expected to change between stable and metastable piles, uncertainties in pile density and viscosity due to heterogeneities (especially along the pile boundary) may make observations more difficult to interpret.

6.3. Manifestation on Earth

Since our models are 2-D, they do not account for 3-D effects, for example an uneven distribution of plumes and non-uniform lateral TBL flow towards the pile margins (Fig. 1). Both factors will affect the symmetry and the amplitude of the topographic features along the LLSVP margin, similar to the variations observed during the plume cycle. A reduced lateral flow, e.g. along sections of the LLSVP margins in between plumes, may result in a smaller and more symmetric short-wavelength CMB topography. In contrast, locally increased and focussed TBL flow towards the roots of plumes (Fig. 1) should cause more pronounced CMB topography, especially at the sites of plume generation. Yet, as long as there is lateral TBL flow towards the piles, a pile with higher intrinsic viscosity should focus stresses into a compressed TBL wedge all along its margins and thus be surrounded by a topographic depression.

Accumulation of stresses at sharp rheological boundaries, as we observe for thermochemical piles with high intrinsic viscosity, may also play a role at the Earth's surface. Rolf and Tackley (2011) studied the influence of continents, or more specifically stiff and stable cratons, on subduction and plate behaviour. Their results show that the presence of sharp viscosity gradients at craton margins focusses stresses and facilitates plate yielding and thus subduction initiation. Although Rolf and Tackley (2011) did not convert these stresses to topography, the underlying process is the same, showing its importance for convective dynamics in different parts of the mantle system. In both cases, the overall topography is likely dominated by flow-related longer-wavelength processes, which may render it difficult to detect features related to compositional viscosity differences. Yet, compared to the complexity of crustal structures and subduction zone dynamics that may mask the circum-cratonic stress signal, the overall structure of the lowermost mantle should be simpler, despite the presence of ultra-low velocity zones (McNamara, 2019). Thus, we would expect to observe a valley with variable depth around the periphery of the LLSVPs if they are indeed thermochemical piles with elevated viscosity.

Patches of ultra-low velocity zones (ULVZs) have been detected seismically, and seem to be associated with LLSVPs, potentially clustering predominantly at pile margins and plume roots (see e.g., review by McNamara, 2019). Similar to the case of LLSVPs, neither the origin nor the density or viscosity of these ULVZ patches are known. Consequently, it is difficult to estimate their effect on our predicted short-wavelength topography. The ULVZs may deepen the circum-pile depression, or prevent its formation, depending on their viscosity and density structure. Furthermore, the depression may help to focus and localize the ULVZ material into distinct patches, keeping most of the material trapped along the margins of the LLSVPs. Yet, independent of the influence of ULVZs on the

short-wavelength CMB topography, we may be able to detect the circum-pile depression in areas where no ULVZ has been observed.

7. Conclusions

Our high resolution thermochemical convection models predict a characteristic short-wavelength topographic depression of about 80–120 km width surrounding the LLSVPs. The depth of this depression depends on the compositional viscosity contrast between the ambient mantle and the pile. Rising plume flow pulls the CMB outside the pile margin upwards, and this effect is more pronounced beneath a high-viscosity pile ($\eta_c > 1$) due to increased coupling between mantle flow and the boundary. This causes relative uplift of the pile-edge maximum compared to the plume-side plateau. Moreover, a wedge of TBL material becomes compressed against a stiff pile and pushes the CMB downwards at the pile edge.

Since the relative amplitude of the depression is small (about 2–4 km in amplitude and 80–120 km wide), this feature is invisible in long-wavelength topography of the CMB and requires high-resolution seismic data. Yet, the valley, if it can be observed, signifies the presence of a compositional viscosity contrast between the LLSVPs and the ambient mantle. The size and symmetry of this topographic structure impose further constraints on the magnitude of compositional viscosity increase, and, to a smaller extent, also on the thermal viscosity contrasts and pile density. The larger the viscosity contrast between pile and mantle, the more pronounced and asymmetric this topography becomes, while increased density or a higher thermal viscosity contrast have the opposite (although considerably smaller) effect. However, the amplitude of relative topography also responds to the (periodic) generation of plumes at the pile edge, with the most prominent (and asymmetric) depression being observed at the time of plume initiation. Consequently, short-wavelength dynamic topography may help to identify regions of active plume generation.

Declaration of competing interest

The authors declare that they have no known competing financial interests or personal relationships that could have appeared to influence the work reported in this paper.

Acknowledgements

Model runtime parameters are listed in Table 1 and Table 2, the code ASPECT is available from (Bangerth et al., 2018). Data for Figs. 6 and 7 can be found in the Supporting Information, Table S1 and S2. We thank Scott King and an anonymous reviewer for valuable feedback on the manuscript, and Miaki Ishii for editorial handling. This work was partly supported by the Research Council of Norway Centres of Excellence project 223272 and through The Norwegian Research School DEEP project 249040/F60. Computation time was provided by the Norwegian computational infrastructure (sigma2) via allocations NN9283K/ NS9029K. We thank the Computational Infrastructure for Geodynamics (geodynamics.org), which is funded by the National Science Foundation under award EAR-0949446 and EAR-1550901, for supporting the development of ASPECT. We further thank Fabio Crameri and Valerie Maupin for helpful discussions about numerical methods, CMB topography, and the seismological potential to detect it.

Appendix A. Supplementary material

Supplementary material related to this article can be found online at <https://doi.org/10.1016/j.epsl.2020.116358>.

References

- Ammann, M.W., Brodholt, J.P., Wookey, J., Dobson, D.P., 2010. First-principles constraints on diffusion in lower-mantle minerals and a weak d'' layer. *Nature* 465, 462–465. <https://doi.org/10.1038/nature09052>. Retrieved from <https://www.nature.com/articles/nature09052#supplementary-information>.
- Austermann, J., Kaye, B.T., Mitrovica, J.X., Huybers, P., 2014. A statistical analysis of the correlation between large igneous provinces and lower mantle seismic structure. *Geophys. J. Int.* 197 (1), 1–9. <https://doi.org/10.1093/gji/gjt500>.
- Ballmer, M.D., Schumacher, L., Lekic, V., Thomas, C., Ito, G., 2016. Compositional layering within the large low shear-wave velocity provinces in the lower mantle. *Geochem. Geophys. Geosyst.* 17 (12), 5056–5077. <https://doi.org/10.1002/2016GC006605>. Retrieved from <https://agupubs.onlinelibrary.wiley.com/doi/abs/10.1002/2016GC006605>.
- Bangerth, W., Dannberg, J., Gassmöller, R., Heister, T., et al., 2018. ASPECT v2.0.1 [Software]. Davis, CA.
- Bangerth, W., Dannberg, J., Gassmöller, R., Heister, T., et al., 2019. ASPECT: Advanced Solver for Problems in Earth's Convection, User Manual.
- Becker, T.W., Boschi, L., 2002. A comparison of tomographic and geodynamic mantle models. *Geochem. Geophys. Geosyst.* 3 (1). <https://doi.org/10.1029/2001GC000168>. Retrieved from <https://agupubs.onlinelibrary.wiley.com/doi/abs/10.1029/2001GC000168>.
- Burmann, F., Noir, J., 2018. Effects of bottom topography on the spin-up in a cylinder. *Phys. Fluids* 30 (10), 106601. <https://doi.org/10.1063/1.5051111>.
- Colombi, A., Nissen-Meyer, T., Boschi, L., Giardini, D., 2014. Seismic waveform inversion for core–mantle boundary topography. *Geophys. J. Int.* 198 (1), 55–71. <https://doi.org/10.1093/gji/ggu112>.
- Conrad, C.P., Steinberger, B., Torsvik, T.H., 2013. Stability of active mantle upwelling revealed by net characteristics of plate tectonics. *Nature* 498, 479–482. <https://doi.org/10.1038/nature12203>. Retrieved from <https://www.nature.com/articles/nature12203#supplementary-information>.
- Davies, D.R., Goes, S., Davies, J., Schubert, B., Bunge, H.-P., Ritsema, J., 2012. Reconciling dynamic and seismic models of Earth's lower mantle: the dominant role of thermal heterogeneity. *Earth Planet. Sci. Lett.* 353–354, 253–269. <https://doi.org/10.1016/j.epsl.2012.08.016>. Retrieved from <http://www.sciencedirect.com/science/article/pii/S0012821X1200444X>.
- Deschamps, F., Li, Y., 2019. Core–mantle boundary dynamic topography: influence of postperovskite viscosity. *J. Geophys. Res., Solid Earth* 124 (8), 9247–9264. <https://doi.org/10.1029/2019JB017859>. Retrieved from <https://agupubs.onlinelibrary.wiley.com/doi/abs/10.1029/2019JB017859>.
- Deschamps, F., Rogister, Y., Tackley, P.J., 2017. Constraints on core–mantle boundary topography from models of thermal and thermochemical convection. *Geophys. J. Int.* 212 (1), 164–188. <https://doi.org/10.1093/gji/ggx402>.
- Ding, H., Chao, B.F., 2018. A 6-year westward rotary motion in the Earth: detection and possible micg coupling mechanism. *Earth Planet. Sci. Lett.* 495, 50–55. <https://doi.org/10.1016/j.epsl.2018.05.009>. Retrieved from <http://www.sciencedirect.com/science/article/pii/S0012821X18302802>.
- Doubrovine, P.V., Steinberger, B., Torsvik, T.H., 2016. A failure to reject: testing the correlation between large igneous provinces and deep mantle structures with edf statistics. *Geochem. Geophys. Geosyst.* 17 (3), 1130–1163. <https://doi.org/10.1002/2015GC006044>. Retrieved from <https://agupubs.onlinelibrary.wiley.com/doi/abs/10.1002/2015GC006044>.
- Dziewonski, A.M., Anderson, D.L., 1981. Preliminary reference Earth model. *Phys. Earth Planet. Inter.* 25 (4), 297–356. [https://doi.org/10.1016/0031-9201\(81\)90046-7](https://doi.org/10.1016/0031-9201(81)90046-7). Retrieved from <http://www.sciencedirect.com/science/article/pii/0031920181900467>.
- Dziewonski, A.M., Lekic, V., Romanowicz, B.A., 2010. Mantle anchor structure: an argument for bottom up tectonics. *Earth Planet. Sci. Lett.* 299 (1), 69–79. <https://doi.org/10.1016/j.epsl.2010.08.013>. Retrieved from <http://www.sciencedirect.com/science/article/pii/S0012821X10005236>.
- French, S.W., Romanowicz, B., 2015. Broad plumes rooted at the base of the Earth's mantle beneath major hotspots. *Nature* 525, 95. <https://doi.org/10.1038/nature14876>. Retrieved from <https://www.nature.com/articles/nature14876#supplementary-information>.
- Gassner, A., Thomas, C., Krüger, F., Weber, M., 2015. Probing the core–mantle boundary beneath Europe and western Eurasia: a detailed study using pcp. *Phys. Earth Planet. Inter.* 246, 9–24. <https://doi.org/10.1016/j.pepi.2015.06.007>. Retrieved from <http://www.sciencedirect.com/science/article/pii/S0031920115000965>.
- Glane, S., Buffett, B., 2018. Enhanced core–mantle coupling due to stratification at the top of the core. *Front. Earth Sci.* 6, 171. <https://doi.org/10.3389/feart.2018.00171>. Retrieved from <https://www.frontiersin.org/article/10.3389/feart.2018.00171>.
- Harpp, K.S., Hall, P.S., Jackson, M.G., 2014. Galapagos and easter: a tale of two hotspots. *Galapagos A Nat. Lab. Earth Sci.* 204, 27–40.
- He, Y., Puckett, E.G., Billen, M.I., 2017. A discontinuous Galerkin method with a bound preserving limiter for the advection of non-diffusive fields in solid Earth geodynamics. *Phys. Earth Planet. Inter.* 263, 23–37. <https://doi.org/10.1016/j.pepi.2016.12.001>.
- Heister, T., Dannberg, J., Gassmöller, R., Bangerth, W., 2017. High accuracy mantle convection simulation through modern numerical methods. II: Realistic mod-

- els and problems. *Geophys. J. Int.* 210 (2), 833–851. <https://doi.org/10.1093/gji/ggx195>.
- Heyn, B.H., Conrad, C.P., Trønnes, R.G., 2018. Stabilizing effect of compositional viscosity contrasts on thermochemical piles. *Geophys. Res. Lett.* 45 (15), 7523–7532. <https://doi.org/10.1029/2018GL078799>. Retrieved from <https://agupubs.onlinelibrary.wiley.com/doi/abs/10.1029/2018GL078799>.
- Heyn, B.H., Conrad, C.P., Trønnes, R.G., 2020. How thermochemical piles can (periodically) generate plumes at their edges. *J. Geophys. Res., Solid Earth*, e2019JB018726. <https://doi.org/10.1029/2019JB018726>. Retrieved from <https://agupubs.onlinelibrary.wiley.com/doi/abs/10.1029/2019JB018726>.
- Koelemeijer, P.J., Deuss, A., Ritsema, J., 2017. Density structure of Earth's lowermost mantle from stoneley mode splitting observations. *Nat. Commun.* 8, 15241. <https://doi.org/10.1038/ncomms15241>. Retrieved from <https://www.nature.com/articles/ncomms15241#supplementary-information>.
- Koelemeijer, P.J., Deuss, A., Trampert, J., 2012. Normal mode sensitivity to Earth's d" layer and topography on the core-mantle boundary: what we can and cannot see. *Geophys. J. Int.* 190 (1), 553–568. <https://doi.org/10.1111/j.1365-246X.2012.05499.x>.
- Koelemeijer, P.J., Schuberth, B., Davies, D., Deuss, A., Ritsema, J., 2018. Constraints on the presence of post-perovskite in Earth's lowermost mantle from tomographic-geodynamic model comparisons. *Earth Planet. Sci. Lett.* 494, 226–238. <https://doi.org/10.1016/j.epsl.2018.04.056>. Retrieved from <http://www.sciencedirect.com/science/article/pii/S0012821X18302656>.
- Kronbichler, M., Heister, T., Bangerth, W., 2012. High accuracy mantle convection simulation through modern numerical methods. *Geophys. J. Int.* 191, 12–29. <https://doi.org/10.1111/j.1365-246X.2012.05609.x>.
- Lassak, T.M., McNamara, A.K., Garnero, E.J., Zhong, S., 2010. Core-mantle boundary topography as a possible constraint on lower mantle chemistry and dynamics. *Earth Planet. Sci. Lett.* 289 (1), 232–241. <https://doi.org/10.1016/j.epsl.2009.11.012>. Retrieved from <http://www.sciencedirect.com/science/article/pii/S0012821X09006591>.
- Lassak, T.M., McNamara, A.K., Zhong, S., 2007. Influence of thermochemical piles on topography at Earth's core-mantle boundary. *Earth Planet. Sci. Lett.* 261 (3), 443–455. <https://doi.org/10.1016/j.epsl.2007.07.015>. Retrieved from <http://www.sciencedirect.com/science/article/pii/S0012821X07004499>.
- Lau, H.C.P., Mitrovica, J.X., Davis, J.L., Tromp, J., Yang, H.-Y., Al-Attar, D., 2017. Tidal tomography constrains Earth's deep-mantle buoyancy. *Nature* 551, 321–326. <https://doi.org/10.1038/nature24452>.
- Le Mouél, J.L., Narteau, C., Greff-Lefftz, M., Holschneider, M., 2006. Dissipation at the core-mantle boundary on a small-scale topography. *J. Geophys. Res., Solid Earth* 111 (B4). <https://doi.org/10.1029/2005JB003846>. Retrieved from <https://agupubs.onlinelibrary.wiley.com/doi/abs/10.1029/2005JB003846>.
- Li, M., McNamara, A.K., 2013. The difficulty for subducted oceanic crust to accumulate at the Earth's core-mantle boundary. *J. Geophys. Res., Solid Earth* 118 (4), 1807–1816. <https://doi.org/10.1002/jgrb.50156>. Retrieved from <https://agupubs.onlinelibrary.wiley.com/doi/abs/10.1002/jgrb.50156>.
- Li, Y., Deschamps, F., Tackley, P.J., 2014. The stability and structure of primordial reservoirs in the lower mantle: insights from models of thermochemical convection in three-dimensional spherical geometry. *Geophys. J. Int.* 199 (2), 914–930. <https://doi.org/10.1093/gji/ggu295>.
- Liu, S., King, S.D., 2019. A benchmark study of incompressible Stokes flow in a 3-d spherical shell using aspect. *Geophys. J. Int.* 217 (1), 650–667. <https://doi.org/10.1093/gji/ggz036>.
- Mancinelli, N., Shearer, P., 2016. Scattered energy from a rough core-mantle boundary modeled by a Monte Carlo seismic particle method: application to pkp precursors. *Geophys. Res. Lett.* 43 (15), 7963–7972. <https://doi.org/10.1002/2016GL070286>. Retrieved from <https://agupubs.onlinelibrary.wiley.com/doi/abs/10.1002/2016GL070286>.
- McNamara, A.K., 2019. A review of large low shear velocity provinces and ultra low velocity zones. In: Linking Plate Tectonics and Volcanism to Deep Earth Dynamics – a Tribute to Trond H. Torsvik. *Tectonophysics* 760, 199–220. <https://doi.org/10.1016/j.tecto.2018.04.015>. Retrieved from <http://www.sciencedirect.com/science/article/pii/S0040195118301586>.
- McNamara, A.K., Zhong, S., 2004. Thermochemical structures within a spherical mantle: superplumes or piles? *J. Geophys. Res., Solid Earth* 109 (B7). <https://doi.org/10.1029/2003JB002847>. Retrieved from <https://agupubs.onlinelibrary.wiley.com/doi/abs/10.1029/2003JB002847>.
- Mulyukova, E., Steinberger, B., Dabrowski, M., Sobolev, S.V., 2015. Survival of llsvps for billions of years in a vigorously convecting mantle: replenishment and destruction of chemical anomaly. *J. Geophys. Res., Solid Earth* 120 (5), 3824–3847. <https://doi.org/10.1002/2014JB011688>. Retrieved from <https://agupubs.onlinelibrary.wiley.com/doi/abs/10.1002/2014JB011688>.
- Restivo, A., Helffrich, G., 2006. Core-mantle boundary structure investigated using sks and skks polarization anomalies. *Geophys. J. Int.* 165 (1), 288–302. <https://doi.org/10.1111/j.1365-246X.2006.02901.x>. Retrieved from <https://onlinelibrary.wiley.com/doi/abs/10.1111/j.1365-246X.2006.02901.x>.
- Roberts, P.H., Aurnou, J.M., 2012. On the theory of core-mantle coupling. *Geophys. Astrophys. Fluid Dyn.* 106 (2), 157–230. <https://doi.org/10.1080/03091929.2011.589028>.
- Rolf, T., Tackley, P.J., 2011. Focussing of stress by continents in 3d spherical mantle convection with self-consistent plate tectonics. *Geophys. Res. Lett.* 38 (18). <https://doi.org/10.1029/2011GL048677>. Retrieved from <https://agupubs.onlinelibrary.wiley.com/doi/abs/10.1029/2011GL048677>.
- Schlaphorst, D., Thomas, C., Holme, R., Abreu, R., 2015. Investigation of core-mantle boundary topography and lowermost mantle with p4kp waves. *Geophys. J. Int.* 204 (2), 1060–1071. <https://doi.org/10.1093/gji/ggv496>.
- Schuberth, B.S.A., Zaroli, C., Nolet, G., 2012. Synthetic seismograms for a synthetic Earth: long-period p- and s-wave traveltimes variations can be explained by temperature alone. *Geophys. J. Int.* 188 (3), 1393–1412. <https://doi.org/10.1111/j.1365-246X.2011.05333.x>.
- Shen, Z., Ni, S., Wu, W., Sun, D., 2016. Short period scp phase amplitude calculations for core-mantle boundary with intermediate scale topography. *Phys. Earth Planet. Inter.* 253, 64–73. <https://doi.org/10.1016/j.pepi.2016.02.002>. Retrieved from <http://www.sciencedirect.com/science/article/pii/S0031920116000200>.
- Soldati, G., Boschi, L., Forte, A.M., 2012. Tomography of core-mantle boundary and lowermost mantle coupled by geodynamics. *Geophys. J. Int.* 189 (2), 730–746. <https://doi.org/10.1111/j.1365-246X.2012.05413.x>.
- Soldati, G., Koelemeijer, P., Boschi, L., Deuss, A., 2013. Constraints on core-mantle boundary topography from normal mode splitting. *Geochem. Geophys. Geosyst.* 14 (5), 1333–1342. <https://doi.org/10.1002/ggpe.20115>. Retrieved from <https://agupubs.onlinelibrary.wiley.com/doi/abs/10.1002/ggpe.20115>.
- Steinberger, B., Holme, R., 2008. Mantle flow models with core-mantle boundary constraints and chemical heterogeneities in the lowermost mantle. *J. Geophys. Res., Solid Earth* 113 (B5). <https://doi.org/10.1029/2007JB005080>. Retrieved from <https://agupubs.onlinelibrary.wiley.com/doi/abs/10.1029/2007JB005080>.
- Steinberger, B., Torsvik, T.H., 2012. A geodynamic model of plumes from the margins of large low shear velocity provinces. *Geochem. Geophys. Geosyst.* 13 (1). <https://doi.org/10.1029/2011GC003808>. Retrieved from <https://agupubs.onlinelibrary.wiley.com/doi/abs/10.1029/2011GC003808>.
- Tackley, P.J., 2012. Dynamics and evolution of the deep mantle resulting from thermal, chemical, phase and melting effects. *Earth-Sci. Rev.* 110 (1), 1–25. <https://doi.org/10.1016/j.earscirev.2011.10.001>. Retrieved from <http://www.sciencedirect.com/science/article/pii/S0012825211001486>.
- Tanaka, S., 2010. Constraints on the core-mantle boundary topography from p4kp-pcp differential travel times. *J. Geophys. Res., Solid Earth* 115 (B4). <https://doi.org/10.1029/2009JB006563>. Retrieved from <https://agupubs.onlinelibrary.wiley.com/doi/abs/10.1029/2009JB006563>.
- Torsvik, T.H., Steinberger, B., Ashwal, L.D., Doubrovine, P.V., Trønnes, R.G., 2016. Earth evolution and dynamics—a tribute to Kevin Burke. *Can. J. Earth Sci.* 53 (11), 1073–1087. <https://doi.org/10.1139/cjes-2015-0228>.
- Trønnes, R.G., Baron, M., Eigenmann, K., Guren, M., Heyn, B., Løken, A., Mohn, C., 2019. Core formation, mantle differentiation and core-mantle interaction within Earth and the terrestrial planets. In: Linking Plate Tectonics and Volcanism to Deep Earth Dynamics – a Tribute to Trond H. Torsvik. *Tectonophysics* 760, 165–198. <https://doi.org/10.1016/j.tecto.2018.10.021>. Retrieved from <http://www.sciencedirect.com/science/article/pii/S0040195118303494>.
- Williams, C.D., Li, M., McNamara, A.K., Garnero, E.J., van Soest, M.C., 2015. Episodic entrainment of deep primordial mantle material into ocean island basalts. *Nat. Commun.* 6, 8937. <https://doi.org/10.1038/ncomms9937>. Retrieved from <https://www.nature.com/articles/ncomms9937#supplementary-information>.
- Wu, W., Ni, S., Shen, Z., 2014. Constraining the short scale core-mantle boundary topography beneath Kenai Peninsula (Alaska) with amplitudes of core-reflected pcp wave. *Phys. Earth Planet. Inter.* 236, 60–68. <https://doi.org/10.1016/j.pepi.2014.09.001>. Retrieved from <http://www.sciencedirect.com/science/article/pii/S0031920114002003>.
- Yang, T., Gurnis, M., 2016. Dynamic topography, gravity and the role of lateral viscosity variations from inversion of global mantle flow. *Geophys. J. Int.* 207 (2), 1186–1202. <https://doi.org/10.1093/gji/ggw335>.
- Yoshida, M., 2008. Core-mantle boundary topography estimated from numerical simulations of instantaneous mantle flow. *Geochem. Geophys. Geosyst.* 9 (7). <https://doi.org/10.1029/2008GC002008>. Retrieved from <https://agupubs.onlinelibrary.wiley.com/doi/abs/10.1029/2008GC002008>.